Article

Theoretical Investigations on the Surface Stability of CuBi$_2$O$_4$ and CuFeO$_2$

Julian Beßner, Stefanie E. Bogenrieder, Robert Neuhoff, Björn Kirchhoff, and Timo Jacob*
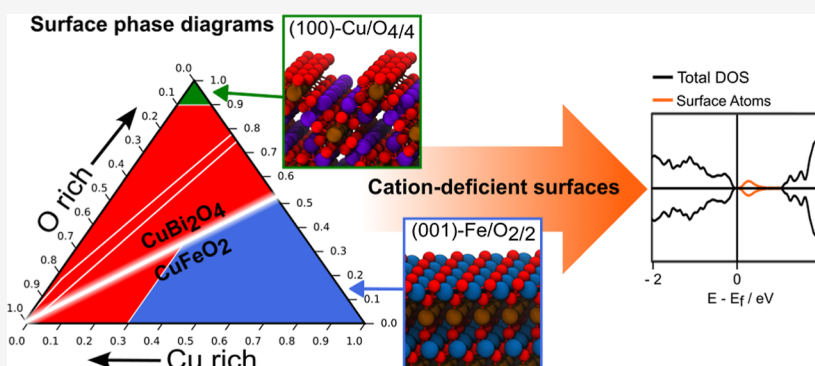
Read Online

ACCESS | Metrics & More | Article Recommendations | Supporting Information

ABSTRACT: CuBi$_2$O$_4$ and CuFeO$_2$ are *p*-type semiconductors that recently have been suggested as profitable photocathode materials for photo(electro)chemical reactions, such as water splitting or carbon dioxide reduction. Currently, not much is known of the surfaces of CuBi$_2$O$_4$ and CuFeO$_2$, although surface properties are crucial for a better understanding of the photocatalytic performance. In this work, we perform electronic structure simulations using DFT + *U* to investigate the structures, electronic properties, and thermodynamic stability of CuFeO$_2$ and CuBi$_2$O$_4$ surfaces. The calculations indicate higher stabilities for stoichiometrically terminated (001)-CuBi$_2$O$_4$ and (012)-CuFeO$_2$ surfaces. Beyond that, the Bader charge analysis of surfaces with Cu-rich terminations yields charge fluctuations among multiple surface layers, giving rise to lower stability of Fe-deficient surfaces. In contrast, both materials' Cu-deficient surface terminations cover greater stability regions. The density of states shows surface states at the valence band maximum and conduction band minimum for cation-deficient surface terminations which can enable the separation of photogenerated electron−hole pairs. These effects could facilitate or complicate higher absorption efficiency for cation-deficient surfaces. Our results emphasize the importance of surface terminations for a better understanding of electronic properties and exhibit further theoretical findings of CuFeO$_2$ and CuBi$_2$O$_4$.

INTRODUCTION

As an abundant and environmentally friendly resource, solar energy has the potential to satisfy the continuously growing energy demands worldwide.[1] Over recent decades, numerous methodologies for taking advantage of solar power have emerged, each displaying diverse technological advancements.[2,3] Among these approaches, one remarkable technique involves the absorption of solar energy and storing it within the chemical bonds of a solar fuel akin to a man-made photosynthesis system.[4] The process of converting solar energy into a chemical fuel within a solid-state device enables a direct utilization of solar energy to drive redox processes. In this configuration, the semiconductor's key role involves absorbing incident photons, creating electron−hole pairs, and easing their separation and transportation.[5] Depending on the application, the semiconductor can be employed as particles ranging from micrometer to nanometer dimensions in a solution or as a photoelectrode.[6] The latter setup typically involves a transparent and conducting oxide material with the

semiconductor deposited as a thin film.[6,7] To accomplish practical-scale photoelectrochemical (PEC) reactions, the photoelectrode should comprise low-cost as well as abundant and nontoxic materials.[2] Semiconducting transition-metal oxides provide a wide array of electronic properties, enabling the possibility of customizing each electrode's band gap and absolute energy level alignment according to the specific electrochemical requirements.
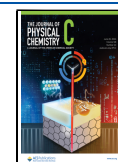
The *p*-type semiconductor copper oxide (Cu$_2$O) has a band gap of 2.17 eV.[8] Furthermore, the conduction band edge position is well-suited for the electron-transfer reactions

associated with the formation of H_2.[9] Unfortunately, Cu_2O electrodes undergo photodegradation in aqueous environments due to the position in the band gap of the redox potentials for the reduction and oxidation of Cu_2O.[10−12] Thus, Cu_2O electrodes are unsuited for PEC devices.

Recently, the focus has shifted toward ternary copper oxides because of their enhanced flexibility in property tuning compared to binary counterparts, gaining attention as potential photocathodes for PEC reduction reactions.[5,13−15] Earth-abundant, stable, and environmentally friendly bismuth oxide materials have been the sought-after goal for developing photocatalytic applications for environmental pollutant degradation, water splitting, and noxious gas reduction.[16−21] The p-type semiconducting behavior is represented in copper oxides.[9] Consequently, combining copper and bismuth oxides to form ternary oxides such as copper bismuth oxide $CuBi_2O_4$ (CBO) yields p-type conductivity.[22] Here, the alloying decreases the rate of CBO self-reduction by guiding the electrons away from the Cu 3d-orbitals. Thereby, the reduced electronic band gap achieves efficient solar absorption.[23]

Besides CBO another promising candidate for photocathode materials is $CuFeO_2$ (CFO) containing Cu^+ ions. Among cuprous delafossites, CFO possesses the smallest band gap (1.1−1.5 eV), consists of earth-abundant elements, and can be prepared by various scalable and low-cost deposition methods.[24−29] CFO is known to produce efficiently hydrogen from water splitting and formic acid from CO_2 reduction.[30,31]

In most studies, only the structural and electronic properties of the bulk phases of CBO and CFO have been investigated.[28,32−34] However, the photocathode's properties are predominantly influenced by their surface properties and so are the PEC reaction processes themselves. The surface provides active sites for PEC reactions and beyond that the essential location for photogenerated charge carrier transfer. Thus, investigating surface terminations is necessary to fully understand the photocatalytic activity of these interesting ternary alloy systems.[35] Therefore, the main focus of this work is to study the surface properties of different CBO and CFO surface orientations, predicting stable terminations and their electronic features. How do these predicted terminations and electronic features contribute to our understanding of surface behavior in materials science? The article is structured as follows. First, we will provide a concise overview of our computational methodology. Subsequently, we will explore the electronic properties of CBO's and CFO's bulk phases and the conditions required for the thermodynamic stability of the CBO and CFO bulk compounds, considering a range of chemical potentials for their constituent elements. Next, we will discuss the electronic structure of diverse surfaces and different terminations, using density of states (DOS) and Bader charge analysis. Finally, we will analyze the stability of the surfaces and their terminations using ternary surface phase diagrams.

METHODS

Theoretical Background. The thermodynamic stability of each surface was evaluated using the *ab initio* atomistic thermodynamics formalism.[36] Here, the surface is assumed to be in equilibrium with an oxygen atmosphere at a fixed temperature and pressure, meaning that the environment acts as a reservoir with a certain chemical potential. To evaluate the thermodynamic stability of each surface morphology, the Gibbs free energy is used

$$\gamma = \frac{1}{2A}\left(G - \sum_i N_i\mu_i\right) \tag{1}$$

where $G = E + pV - TS$ with the internal energy E, pressure p, volume V, temperature T, and entropy S. N_i is the number of atoms in the system, and μ_i is the chemical potential of species i, respectively. The Gibbs free energy is normalized to the surface areas of the two surfaces of the symmetric slab model. Due to the small contribution of the terms pV and TS, the terms are negligible, as shown in literature.[9,36,37] Hence, the Gibbs free energy is described by the total DFT energy of the system, and eq 1 changes to

$$\gamma = \frac{1}{2A}\left(E - \sum_i N_i\mu_i\right) \tag{2}$$

where E is the calculated total energy of the system.[36,38,39] Using eq 2, the surface energy calculation of nonstoichiometric surfaces is possible.[40] Due to the thermodynamic equilibrium between the surface and the bulk material, the following stability condition for CFO arises

$$\mu_{CFO}^{bulk} = \mu_{Cu} + \mu_{Fe} + 2\mu_O \tag{3}$$

μ_{CFO}^{bulk} depends on the experimental conditions, but it can be approximated as the total energy E_{CFO}^{bulk} per formula unit of the bulk phase at $T = 0$ K and $p = 0$ atm.[36] Here, it is directly derived from our DFT calculations. Thus, there are only two independent chemical potentials remaining. Additionally, the chemical potentials μ_i of the three species in the ternary oxide are referenced to the energy in their respective bulk/gaseous reference phases

$$\mu_{Cu} = E_{Cu}^{GGA+U} + \Delta\mu_{Cu}, \quad \mu_{Fe} = E_{Fe}^{GGA+U} + \Delta\mu_{Fe},$$
$$\mu_O = \frac{1}{2}E_{O_2}^{GGA+U} + \Delta\mu_O(T,p) \tag{4}$$

The chemical potential of oxygen is calculated by its zero-temperature energy term (from DFT) plus a correction $\Delta\mu_O(T,p)$, depending on the temperature and pressure

$$\Delta\mu_O(T,p) = \Delta\mu_O^0(T,p_0) + \frac{1}{2}k_BT\ln\left(\frac{p}{p_0}\right) \tag{5}$$

where $\Delta\mu_O(T,p)$ depends on temperature and pressure through the ideal gas law. The chemical potential values of oxygen at 1 atm are obtained from the thermochemical data reported in the NIST-JANAF database.[41]

Therefore, eq 3 transforms into

$$\Delta\mu_{CFO}^{bulk} = \Delta\mu_{Cu} + \Delta\mu_{Fe} + 2\Delta\mu_O \tag{6}$$

where $\Delta\mu_{CFO}^{bulk} = E_{CFO}^{bulk} - E_{Fe}^{GGA+U} - E_{Cu}^{GGA+U} - E_O^{GGA+U}$ is the change of the Gibbs free energy of formation of bulk CFO from bulk metal Fe, bulk metal Cu, and gaseous O_2.

Combining eqs 3 and 6 and choosing the chemical potentials $\Delta\mu_{Cu}$ and $\Delta\mu_O$ to be independent, then eq 2 gives

$$\gamma = \frac{1}{2A}(E - N_{Fe}E_{CFO}^{bulk} - (N_{Cu} - N_{Fe})(\Delta\mu_{Cu} + E_{Cu}^{GGA+U})$$
$$- (N_O - 2N_{Fe})(\Delta\mu_O + E_O^{GGA+U})) \tag{7}$$

To guarantee that CFO does not decompose into Cu and Fe bulk metals as well as O_2, the following conditions for the chemical potentials must be satisfied

$$\Delta\mu_{CFO}^{bulk} \leq \Delta\mu_{Cu} \leq 0,$$

$$\Delta\mu_{CFO}^{bulk} \leq \Delta\mu_{Fe} \leq 0, \text{ and}$$

$$\frac{1}{2}\Delta\mu_{CFO}^{bulk} \leq \Delta\mu_{O} \leq 0 \qquad (8)$$

The inequalities eq 8 are derived from eq 6. The upper boundaries of $\Delta\mu_i$ are also known as the *i*-rich environment because a higher value of the chemical potential corresponds to a higher concentration of the *i*th species.[36]

Besides decomposition into pure bulk metals, the decomposition into binary bulk metal oxides must also be assessed. As an example, the formation energy from Cu bulk metal and O_2 gas to bulk CuO is $\Delta\mu_{CuO}^{bulk} = \mu_{CuO}^{bulk} - E_{Cu}^{GGA+U} - E_{O}^{GGA+U}$. Here, μ_{CuO}^{bulk} can be approximated by the energy per unit formula of the bulk phase, which is directly obtained from DFT calculations at $T = 0$ K and $p = 0$ atm for all the bulk systems. If the equation

$$\Delta\mu_{Cu} + \Delta\mu_{O} \leq 0 \qquad (9)$$

is satisfied, then the decomposition of CFO into CuO is restricted. This analysis was carried out for Cu_2O, FeO, Fe_2O_3, and Fe_3O_4, which is reported in the Supporting Information.

To derive the thermodynamically most stable surface composition and geometry, one has to minimize γ from eq 7. The surface energy can be plotted in a ternary surface phase diagram, showing only the lowest surface energy values for a set of triplets of chemical potentials ($\Delta\mu_O$, $\Delta\mu_{Cu}$, and $\Delta\mu_{Fe}$).[40]

Computational Settings. The Vienna ab initio simulation package (VASP) version 6.2 was employed to facilitate DFT-based electronic structure spin-polarized simulations, utilizing the projector augmented wave approach.[42−46] The Perdew−Burke−Ernzerhof (PBE) exchange−correlation functional, augmented with Hubbard *U* corrections (PBE + *U*), was applied to estimate the exchange−correlation potential.[47,48] The influence of localized Cu-3d, Fe-3d, and Bi-5d orbitals in CFO and CBO has a mitigating effect on the Coulombic interaction in the context of PBE.[49,50] To handle the strongly correlated orbitals of the d electrons of the materials, the DFT + *U* method with the rotationally invariant formulation of Dudarev was employed for the d electrons of Cu ($U = 8$ eV), Fe ($U = 4$ eV), and Bi ($U = 8$ eV).[48] The chosen *U* values were determined by investigating the lattice parameter, the magnetic moment, and the band gap of CFO and CBO for various values of the Hubbard *U* parameter, as reported in the Supporting Information (Tables S1 and S2). After comparing the results to experimental and theoretical data, the closest representation was used for all further calculations.[22,28,34,51,52] Thus, the *U* values are in agreement with the published values for mixed transition-metal oxides.[31,32,53]

A Monkhorst−Pack grid was chosen according to a $\vec{k}$-spacing of at least 0.16 to sample the Brillouin Zone during the full structural relaxation and optimization until the Hellmann−Feynman forces and self-consistent total electronic energy convergence reached below values of 10^{-3} eV·A^{-1} and 10^{-5} eV, respectively. The DOS was visualized with the help of VASPKIT[54] and was evaluated with a total electronic energy convergence criteria of 10^{-6} eV and a denser $\vec{k}$-point grid of at least 0.08. The plane wave cutoff was set to 500 eV for both materials. The exact $\vec{k}$-point grid for each system can be found in the Supporting Information (S3 and S4). To prevent the creation of a net dipole moment within the unit cell, symmetric

slabs with two identical terminations were employed to model the surfaces. Additionally, the slabs were padded with a 10 Å vacuum region added in the direction perpendicular to the surface to avoid artificial interactions between periodic replicas.

Furthermore, Bader charge analysis was performed for all surfaces to investigate the charge distribution among the surface atoms and the effect on the surface stability.[55] We have investigated the (110), (100), (111), (001), and (012) surfaces for CFO and (110), (100), and (001) surfaces for CBO. The side views of the geometries have been created with the VMD[56] molecular graphics viewer.

■ RESULTS AND DISCUSSION

Structural and Electronic Properties of CBO and CFO. The calculated lattice parameters of CFO yield $a = 3.057$ Å and $c = 17.250$ Å, while CBO crystallizes with lattice parameters of $a = 8.517$ Å and $c = 6.205$ Å. The corresponding unit cells of the two materials are shown in Figure 1. CBO
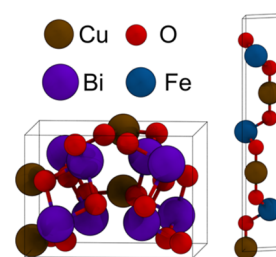

Figure 1. Unit cells of CBO (left) and CFO (right). Cu atoms are colored brown, Fe atoms in blue, Bi atoms are purple, and O atoms are red.

comprises square-planar $[CuO_4]^{6-}$ units stacked along the *c*-axis, with Bi^{3+} ions in-between the stacks and coordinated to six O^{2-}. The Cu−O bonds within the $[CuO_4]^{6-}$ units are at 1.946 Å, and the Bi−O bonds are at 2.260 and 2.433 Å, respectively. In contrast to CBO, CFO belongs to the Cu(I)-based oxides with two alternating layers. It comprises a planar layer of Cu cations, arranged in a triangular pattern, and a layer of edge-sharing FeO_6-distorted octahedra, where each O^{2-} ion is coordinated by one Cu^+ and three Fe^{3+} cations. The Cu−O and Fe−O bond lengths are at 1.846 and 2.018 Å, respectively. There are two possibilities for stacking the FeO_6 octahedra, leading to two different crystal structures: the rhombohedral ($R\bar{3}m$) and the hexagonal ($P6_3/mmc$) space groups. In this work, we focus on the rhombohedral structure of CFO, which is often used in experimental studies.[57,58]

The calculated structural parameters of CFO and CBO are summarized in Table 1. Using the GGA + *U* approach, the CBO's lattice parameter $c = 6.205$ Å is overestimating the

Table 1. Lattice Parameters and Bond Lengths Calculated for Both Materials, Using the DFT + *U* Approach

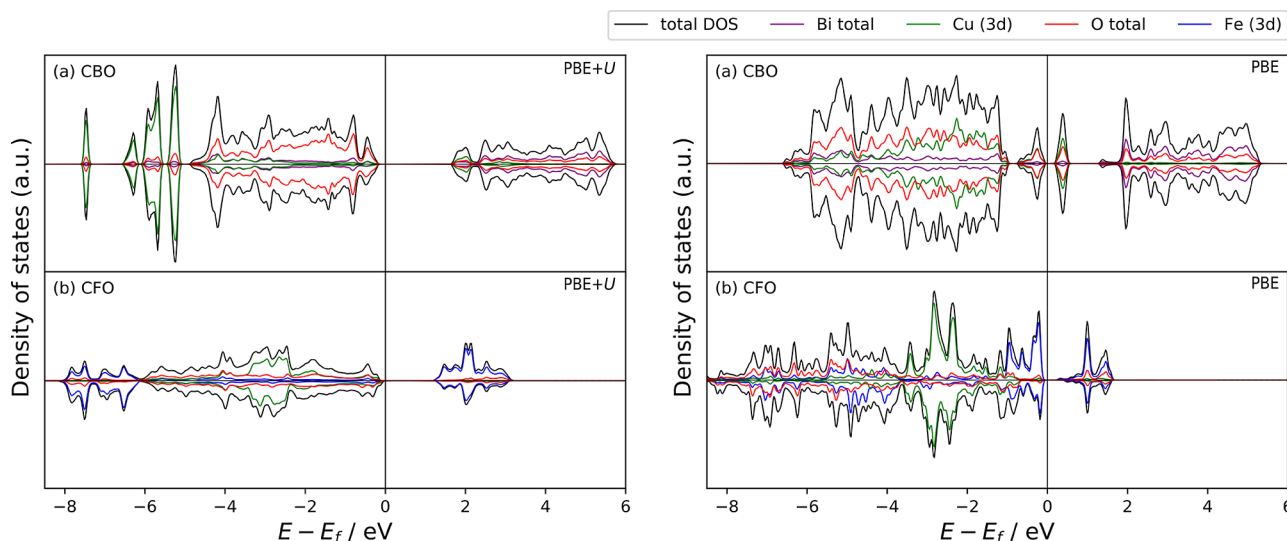| material	method	a/Å	c/Å	band gap/eV
CFO	this work	3.057	17.250	1.33
CFO	DFT + *U*	3.060[29]	17.21[29]	1.36[31]
CFO	exp.	3.034[57]	17.162[57]	1.43[28]
CBO	this work	8.517	6.205	1.91
CBO	DFT + *U*	8.494[22]	6.025[22]	1.90[59]
CBO	exp[32]	8.481	5.807	1.80

Figure 2. DOS of the CBO (a) and CFO (b) bulk system calculated with PBE (left) and PBE + U (right).

experimental value of 5.807 Å.[32] This overestimation is well-known as the PBE-functional tends to underbind the atoms in the unit cell.[32] Additionally, the Hubbard U parameter can increase the lattice parameters as well.[60] Nevertheless, the lattice parameters of CFO agree with the equilibrium lattice constants obtained experimentally and theoretically at the PBE + U level of theory.[28,31]

The photocatalyst's optical band gap should fall within the visible light spectrum to fulfill the essential requirement for an effective conversion of solar energy. Figure 2 compares the DFT and DFT + U calculations of CFO and CBO.

The valence band of CBO calculated by PBE + U is composed of narrow Cu-3d states at −7.5 and −6.5 to −5 eV. For energy values higher than −5 eV, the Cu-3d states and the Bi-5d states are weaker, while the O-2p states are dominant between −5 and 0 eV. In contrast, the Cu-3d and O-2p states calculated by PBE are diffused between −6 and −1 eV. Additionally, an isolated narrow state in the valence band maximum arises. This mixed state results from significant hybridization between Cu-3d and O-2p orbitals, accompanied by minor contributions from Bi orbitals. In the conduction band of the DOS calculated by PBE, a narrow state at 0.45 eV is characterized by strong interactions between Cu-3d and O-2p orbitals as well. The two narrow states yield a small band gap of 0.37 eV, confirming the well-known underestimation of PBE in describing band gaps.[61]

In the conduction band calculated by PBE + U, there is an equal contribution of states between O and Bi. The empty Cu-3d states are only present in the conduction band minimum at 1.91 eV. The O-2p and Cu-3d states interact, leading to a dominant contribution at 1.95 eV. At higher energy values, the Bi-6p states have a significantly higher contribution to the conduction band. The contribution of the Cu-3d states at the valence band maximum and the conduction band minimum mainly originates from the Cu-$3d_{x^2-y^2}$ states that are hybridized with the O-sp^3 orbitals in the square-planar $[CuO_4]^{6-}$ units. Thus, the lowest-energy optical absorption is provided by the Cu d−d excitation and not by the O-2p to Cu-3d transition. However, the efficiency of d−d transitions is known to be lower in converting photons to photocurrent compared to O^{2-} ligand to metal cation charge-transfer transitions.[22] Higher

energy values are necessary to generate a significant photocurrent efficiency, leading to an optical absorption corresponding to the O-2p to Cu-3d transition.[51]

Moreover, the $[CuO_4]^{6-}$ units are isolated from each other in the bulk with a minimal distance of 3.10 Å between the Cu atoms in two neighboring $[CuO_4]^{6-}$ units. As a consequence, the photogenerated electrons and holes are localized in the $[CuO_4]^{6-}$ units, giving rise to a deceleration of the charge carriers and the formation of polarons. The polaron formation can be seen in the PDOS as the states in the conduction band minimum are almost segregated from the states larger than 2 eV in the conduction band. The small polaron hopping is widely discussed in the literature as the main reason for the poor charge carrier transport in CBO.[5,33,62]

Introducing the U parameter to Cu and Bi gives a larger band gap of 1.91 eV, now laying within the range of 1.5−2.11 eV as reported in experimental and theoretical studies.[22,33,51,63] Additionally, the nature of the magnetization of CBO is antiferromagnetic with an absolute magnitude of the magnetic moment of 0.68 μ_B for the Cu atoms, which is in agreement with neutron diffraction measurements and DFT + U calculations.[22,64] This manuscript provides fundamental results for follow-up studies on surface reactions, and how these are influenced by the magnetic properties of the materials and their surfaces. Hence, we will not elaborate any further on magnetization for both materials as there are already a lot of publications covering this topic.[34,65−68] Literature has shown that applying the Hubbard parameter to the Cu-3d and Bi-5d states enhances the Coulombic interaction of both Cu-3d and Bi-5d states, thus increasing the band gap to a value in agreement with experiments.[32] As indicated in Table 1, experimental studies can yield lower band gap values of 1.5−1.8 eV which could be a consequence of Cu defects in the material.[59,61]

For CFO, the valence band mainly consists of Cu-3d states at −3.5 eV and hybridized Fe-3d states at −8 to −6 eV. These hybridized Fe states occur only in the DOS calculated on the DFT + U level. In the DOS calculated without the U parameter, the Fe-3d states are distributed over the valence band with states at −5 eV and from −1 to 0 eV. The Fe states are thus more separated when using the DFT + U approach. In
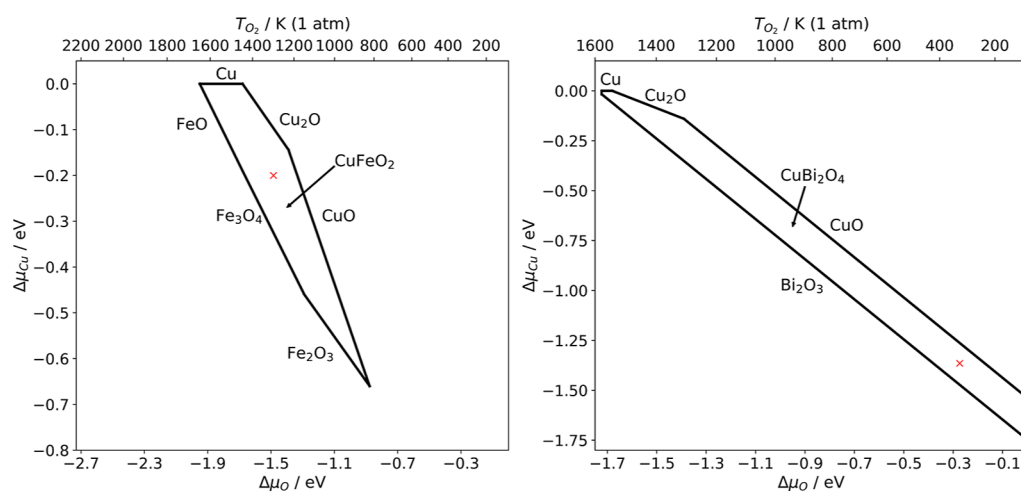
Figure 3. Stability region of the bulk system of CFO (left) and CBO (right) and the equilibrium lines with other Cu−Fe−O and Cu−Bi−O materials as a function of the chemical potential of Cu and O. The red cross represents the point at which the chemical potentials have been chosen to compute the surface energy values for all investigated surface terminations, as shown in Tables S5 and S6.

both methods, the O-2p states cover the DOS from −7 to 0 eV.

The conduction band of the DOS with and without the U parameter is predominantly composed of empty Fe-3d states. Only very weak contributions of O states can be seen for higher energy values in the conduction band. This agrees with previously reported experimental and theoretical studies.[28,31,69] In the DOS calculated by DFT + U, the Fe-3d states cover a larger region from 1.33 to 3 eV. The lowest optical transition is thereby achieved by an electron excitation from O 2p states to Fe-3d states. Studies suggest that the electron excitation is followed by an electron transfer from Cu-3d states to deeper O-2p states, facilitating the charge separation process in the surface.[70] This effect enhances the charge carrier lifetime and improves the stability significantly compared to the binary oxide Cu_2O.[30] Despite the longevity of excited electrons in CFO, studies indicate a self-trapping effect due to polaron hopping, which is based on an electron excitation into a Fe-3d orbital in the conduction band.[71] Consequently, a reduction of Fe^{3+} to Fe^{2+} occurs, leading to a change in the Fe−O bond length.[71]

For CFO, the DFT + U approach yields a band gap of 1.33 eV, which agrees with experimental and theoretical values reported in literature.[28,31,52] However, the band gap calculated without the U parameter almost yields a metallic character. Thus, applying Hubbard corrections is required for realistic predictions of the semiconducting behavior of both materials. Furthermore, the presence of lower-energy Fe-3d orbitals accounts for the smaller band gap observed in CFO compared to other delafossite compounds.[72] The absolute magnitude of the magnetic moment for the Fe atoms in CFO is 4.27 μ_B, which is also reported in literature.[34,69,73]

Stability Regions of CBO and CFO. The synthesis of ternary oxides strongly depends on the stability of the corresponding binary metal oxides. Therefore, the decomposition into different metal oxides or pure elemental phases needs to be addressed. The probability of decomposition in competing compounds can be minimized by controlling the chemical potentials as in (eq 9), which directly correspond to temperature and pressure. Figure 3 shows the stability region for CBO and CFO, respectively. The axes represent the referenced chemical potential $\Delta\mu_{Cu}$ between the copper in

CBO or CFO and the metallic bulk reference phase. The upper horizontal axis shows the temperature in Kelvin, corresponding to the chemical potential of oxygen. The lines depict the borders of the thermodynamic stability region for each bulk phase.

The area above the copper oxide lines is favorable for decomposition into CuO and Cu_2O, respectively. The region below the lines, corresponding to the binary iron oxides FeO, Fe_2O_3, and Fe_3O_4 indicates decomposition into these iron oxides. This leaves an area from about 800 K to almost 1700 K as the stability region for the CFO. According to the calculated stability region, CFO forms at higher temperatures, but there are also experimental studies showing CFO exists at ambient temperatures, probably as meta-stable phase.[66,74] This observation indicates the existence of a high energy barrier, preventing the decomposition of CFO to its binary oxide compounds.

The calculated stability region is larger than what has been reported in experimental studies so far.[57,75] The larger stability region in our work mainly results from the chosen U parameters, resulting in different Gibbs free energy of formation values of the binary iron and copper oxides.[52] Furthermore, it is important to note that the selected U parameter for Cu and Fe in the ternary copper oxide may not be optimal for their respective metallic phases as these parameters are primarily chosen for the CFO phase.[76] Besides, in experimental papers diverse Fe/Cu stoichiometric phases, liquid phases, and solid spinel phases have also been considered, while here we concentrate on the solid stoichiometric phases only.[57,75] Moreover, the overbinding issue of GGA for the oxygen molecule has not been addressed in our work, which would influence the Gibbs free energy of formation for the bulk oxides as well.[77,78] However, despite the limitations of PBE + U, the relative stability of competing phases is in agreement with literature.[57,79]

Most experimental articles describe phase diagrams for Bi_2O_3−CuO systems or similar two- or three-component systems.[80−84] They all consider different stoichiometric mixtures and liquid phases, making it difficult to compare the same stability region of solid stoichiometric CBO.

There are ternary oxides containing bismuth, for example, $BiFeO_3$ (BFO), showing also a narrow and elongated stability
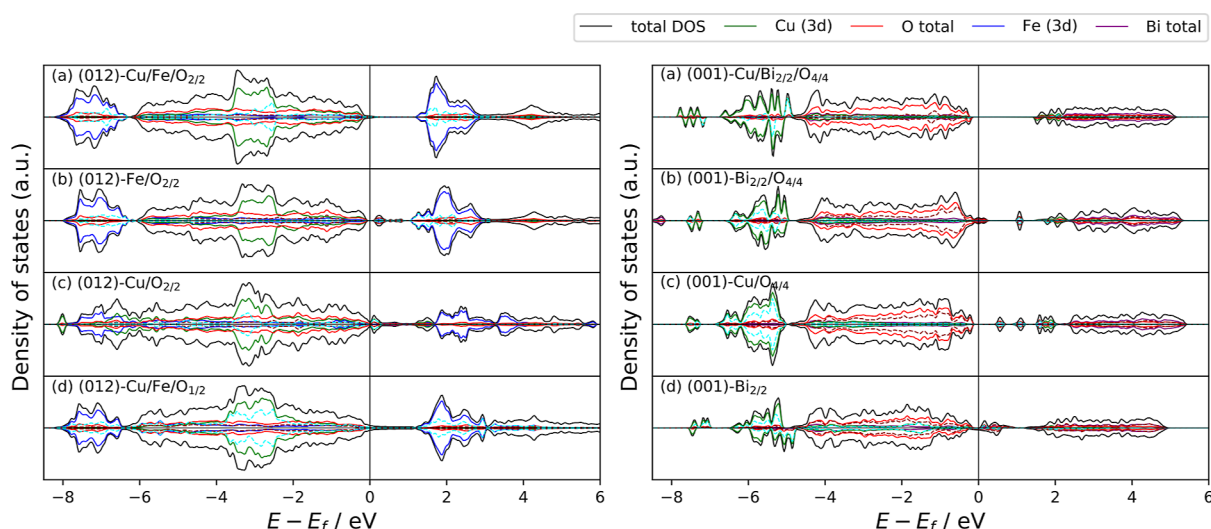
Figure 4. DOS of the (012)-CFO and (001)-CBO surfaces with different terminations. The dashed lines represent the contribution of the 3d (light blue) states of Cu/Fe atoms and p states (brown) of O/Bi atoms in the outermost surface layer.

region.[85] Bi_2O_3 shows thermodynamically higher stability than other bismuth oxides; thus, it creates the lower boundary for the stability region. Only at high temperatures, Cu_2O sets the stability region of CBO, below 1300 K CuO creates the upper boundary for the stability region. The narrow stability region indicates that the heat of reaction between Bi_2O_3 and CuO is small, and CBO is borderline.

The stability region of CBO gives rise to high stability even under strongly oxidizing conditions ($\Delta\mu_O = 0$) and therefore ambient conditions, as reported in literature as well.[86] While lower temperatures create smaller particles and poorly crystallized products, higher temperatures of 1200 K facilitate larger grain growth.[32,81,86,87] The narrow stability region complicates the synthesis of a pure CBO phase, leading to grains with different Cu/Bi ratios. Moreover, the binary and nonstoichiometric oxides are photoelectrochemically active, providing different electronic and optical properties. Thus, the position of the valence and conduction bands, hence the band gap value, can easily differ, depending on the Cu/Bi ratio.[88]

Electronic Properties of CBO and CFO Surfaces. Figure 4 shows the total density of states (TDOS) and its projection onto relevant orbitals for different terminations of the (012) and (001) surfaces of CFO and CBO, respectively. These surfaces were chosen because of their higher stability compared to others, as will be discussed in the next section. The annotation located in the corners depicts the constituent elements present on the surface for this particular termination. Additionally, the numbers in the index describe the ratio of the corresponding element in the surface. Thereby, surface terminations, containing half the number of oxygen atoms, can be expressed. The side views of the geometries in the Supporting Information may give a better insight into the annotation.

The PDOS of CFO in Figure 4 is symmetric for all terminations, reflecting the antiferromagnetic ordering of the Fe atoms in the symmetric slab. The $Fe/O_{2/2}$ and $Cu/O_{2/2}$ terminations of CFO, as shown in the left Figure 4b,c respectively, indicate metallic behavior. There are small p and d states within the band gap. The metallic character of those terminations is a consequence of the loss of the Cu/Fe/O stoichiometry. Specifically, as depicted by the dashed lines in

Figure 4, these peaks demonstrate the delocalization among the O atoms within the outermost O–Fe–O and O–Cu–O layers. The metal-deficient terminations create an excess of holes due to the surface's missing Cu or Fe atoms. The formation of the midgap states provided by the charge reorganization is known to be a possible mechanism for sustaining polar surface layers.[89,90] Due to the proximity of the midgap states to the Fermi level, a partial occupation of the p and d states can be suggested.

On the contrary, an oxygen deficiency in the outermost layer could provide the opposite charge for the missing cations, resulting in compensation of the excess holes and loss of the metallic character in the slab, as shown in Figure 4d. Hence, introducing Cu or Fe vacancies and interstitial oxygen can alter the PEC performance.[30] In particular, Cu vacancies enhance the PEC efficiency by facilitating the generation of electron–hole pairs.[30] The rapid delocalization of photogenerated holes creates the charge separation to Cu-3d and O-2p states.[70] The surface states in the metal-deficient surfaces are mainly composed of Cu- and Fe-3d states, suggesting that Cu and Fe atoms act as the functional sites on the surface. Thereby, surface states near the Fermi level decrease the band gap and enhance the surface's reactivity for photocatalytic reactions.

The stoichiometric and O-deficient terminated surfaces show a typical DOS plot for a semiconductor. The missing states in the band gap and at the Fermi level are due to non-existent holes in the stoichiometric termination and the non-delocalized charge in the O-deficient termination in the outermost layer. Therefore, no redistribution of charge is necessary to stabilize the surfaces.

The DOS for the (111), (110), (100), and (001) surfaces are reported in the Supporting Information. The cation-deficient surface terminations show similar behaviors in the band gap. The generated holes in the cation-deficient surfaces are then delocalized among surface atoms, giving rise to peaks at the Fermi level and above.

For CBO, the stoichiometrically terminated (001) surface exhibits a similar DOS to the bulk's DOS in Figure 2, indicating equal electronic properties as in the bulk. The Cu-3d states are located in the conduction band minimum, and the O-2p states are at the valence band maximum. In the band gap,
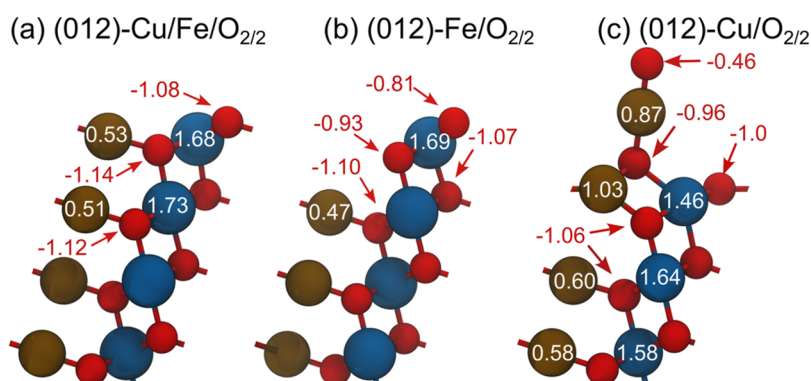
Figure 5. Side views of the Cu/Fe/$O_{2/2}$-, Cu/$O_{2/2}$-, and Fe/$O_{2/2}$-termination of the (012)-CFO surface. The values on the atoms show their Bader net charges. Atoms without a value have the same Bader net charges as in the bulk.

there are no states present. The Cu-deficient surface, as shown in Figure 4b, features states comprising 3d and 2p orbitals in the band gap. The dashed lines indicate that the states are formed by the Cu and O atoms in the outermost layers. Cu vacancies on the surface can lead to partially empty states in the valence band. Similarly to CFO, the loss of the stoichiometry generates an excess of holes in the surface, providing O-2p states at the Fermi level and above. The small states within the band gap at 1.1 eV belong to the $[CuO_4]^{6-}$ unit within the subsurface layer. As suggested in literature, these $[CuO_4]^{6-}$ units serve as conduction paths for the photogenerated holes and electrons.[62] Compared to the DOS of the bulk, these states are completely isolated from the conduction band, leading to localization of electrons at the $[CuO_4]^{6-}$ unit in the subsurface layer. The midgap states are stabilized at lower energy values compared to the conduction band minimum in the bulk's DOS, which supports the formation of polarons. The Cu/$O_{4/4}$-terminated surface exhibits states within the band gap as well. Here, the isolated states within the band gap originate from the $[CuO_4]^{6-}$ units too. Like for the $Bi_{2/2}$/$O_{4/4}$-terminated surface, the conduction band minimum in the Bi-deficient surface termination is completely separated from the rest of the conduction band. Beyond that, the states are shifted to lower energy values, depending on the position of the $[CuO_4]^{6-}$ within the slab. The surface states at 1.7 eV belong to the outermost $[CuO_4]^{6-}$ unit, while $[CuO_4]^{6-}$ in the subsurface layer and deeper provide the other two isolated surface states at around 1.0 and 0.5 eV, respectively. Hence, the polaron formation at the $[CuO_4]^{6-}$ sites can be stabilized further beneath the surface.

The $Bi_{2/2}$-terminated surface in Figure 4d provides Bi-6p and O-2p states above the Fermi level due to the under-coordination of the Bi atoms on the surface. Unlike in the $Bi_{2/2}$/$O_{4/4}$-terminated surface, the isolated Cu and O states are shifted to lower energy values near the Fermi level, giving rise to a delocalization of charge between the Bi atoms and the $[CuO_4]^{6-}$ unit in outer layers.

The DOS for the (110) and (100) surfaces are reported in the Supporting Information. The formation of midgap states in the Cu/$O_{4/4}$- and Bi/$O_{4/4}$-terminated surfaces is similar to the (001) surface, depending on the surface cleavage of the orientation and the coordination of the $[CuO_4]^{6-}$ units changes, leading to different positions of the isolated states.

The asymmetry of the PDOS, especially in the (001) surface of CFO in the Supporting Information, is caused by the dangling bonds in the outermost layers, indicating higher reactivity.[35] Additionally, the DOS for the (001) surface of CFO shows a metallic character, emphasizing the fast recombination of photogenerated electron–hole pairs from the conduction band to the valence band.[35] Thus, the surface and its termination have to be chosen carefully as this can limit the photocatalytic performance.

Moreover, a Bi-terminated surface gives rise to peaks at the Fermi level and above. This metallic character can be seen in the (110) and (100) surfaces of CBO reported in the Supporting Information as well.

Furthermore, we calculated the Bader charges for different surfaces of CFO and CBO. Figure 5 shows the Bader net charges of the stoichiometrically terminated (a), the Fe/$O_{2/2}$-terminated (b), and the Cu/$O_{2/2}$-terminated (012) surfaces of CFO. In the bulk phase, Cu, Fe, and O atoms have a Bader net charge of 0.51, 1.74, and −1.13 e, respectively. According to the coordination environment, this indicates a charge transfer of 0.26 e from a Cu atom and 0.28 e from a Fe atom to an adjacent O atom. Comparing the bulk values with the charges in the stoichiometrically terminated surface in Figure 5a, we can see that the charges of the surface atoms are converged to the charges of the bulk atoms within the outermost layer. A similar charge distribution gives rise to the same charge transfer in the stoichiometric surface and the bulk. The charge values for the Cu atoms can also be found in other delafossites.[72] The charge distribution for the Fe/$O_{2/2}$-terminated surface is very similar to the stoichiometrically terminated surface. Here, the outermost O atoms are unsaturated, leading to a more positive charge of −0.81 e. Thus, the charge transfer of the cations to the O atoms on the surface is less, indicating partially unoccupied states.

The charges in the Cu/$O_{2/2}$-terminated surface differ from the bulk values, even in deeper layers of the slab. The missing coordination environment of the outermost O atom leads to a lower negative charge transfer of −0.46 e as the outermost Cu atom is the only bound atom. To keep the negative charge at the O atoms, the O atom in the subsurface with a charge of −0.96 e moves closer to the neighboring Cu atom, which results in a change in the coordination number of the Cu atom from two to three. Hence, this Cu atom is bound to three O atoms and doubles its charge to 1.03 e. The two outer Cu atoms have a change in their Bader net charge of at least 0.30 and 0.50 e, respectively, giving rise to a change of the oxidation state from Cu$^+$ to Cu^{2+}.[91] The oxidation of the outer Cu atoms
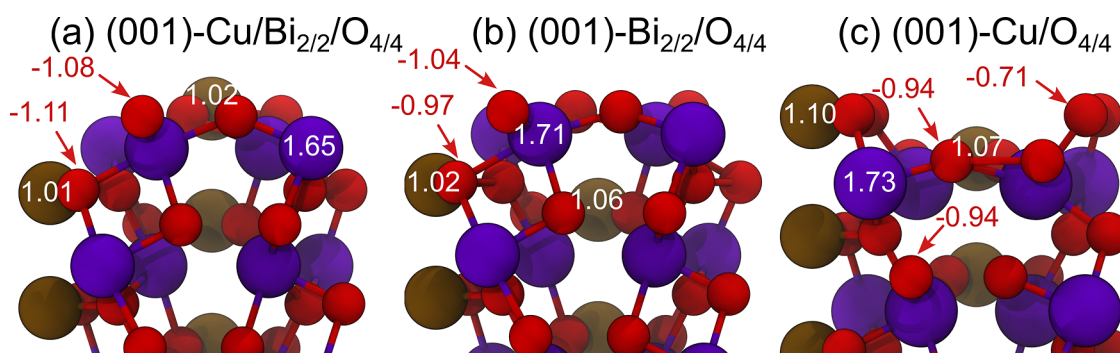
Figure 6. Side views of the $Cu/Bi_{2/2}/O_{4/4}$-, $Cu/O_{4/4}$-, and $Bi_{2/2}/O_{4/4}$-termination of the (001)-CBO surface. The values on the atoms show their Bader net charges. Atoms without a value have the same Bader net charges as in the bulk.
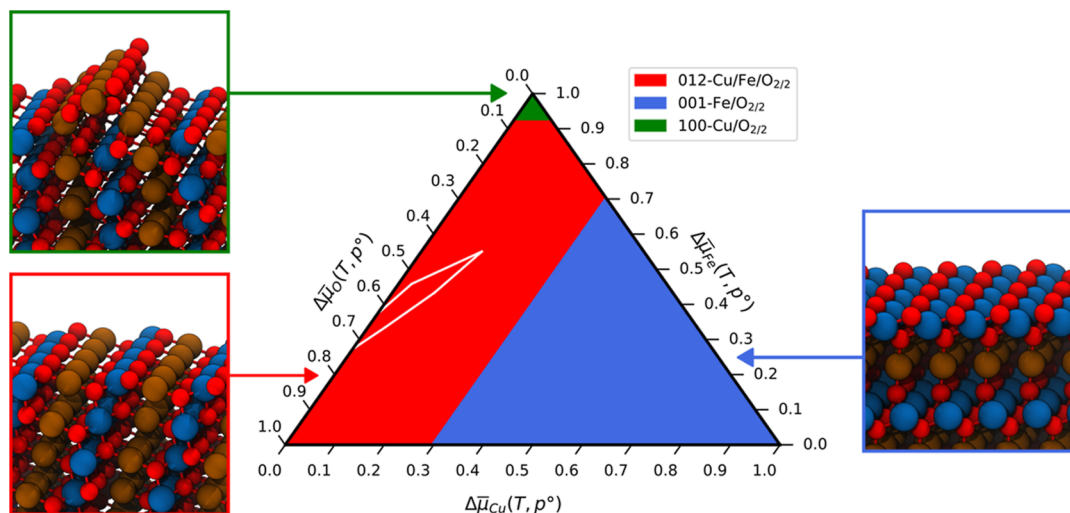

Figure 7. Ternary surface phase diagram for CFO with the stability region and the optimized geometries of the most stable surface terminations. Each colored area in the ternary diagram represents the surface with the lowest surface energy.

generates partially empty states of the outer surface Cu atoms, confirming the midgap states above the Fermi level in the PDOS in Figure 4c. The higher charge of the Cu atoms is then compensated by the Fe atom's lower Bader net charge. As a result, charge fluctuations are present in at least four layers deep in the surface slab. Depth profiling X-ray photoelectron spectroscopy measurements support the higher concentration of Cu^{2+} ions in surface layers, while Cu^+ ions are more present in the bulk phase of CFO.[30,92]

In the Supporting Information, the Bader charge distribution for the (110), (001), (111), and (100) surfaces are reported as well. For these surfaces, the charge distribution is very similar compared to the (012) surface. The Fe-deficient surface terminations lead to surfaces containing Cu^{2+} ions in the outer layers and charge fluctuations across multiple layers, while the Cu-deficient surfaces show less disturbed charge distributions compared to the bulk values. Beyond that, all the stoichiometric terminations of the surfaces exhibit bulk-like charge distributions, providing higher stabilities as we will see in the last section.

Additionally, we analyzed the Bader charges for different surface terminations of CBO, as shown in Figure 6. The bulk's Bader net charge values for Cu, Bi, and O are 1.02, 1.69, and −1.10 e, respectively. Thus, the O atoms receive a net charge of 0.25 e of the Cu atom and 0.85 e of the surrounding Bi atoms. The Bader net charges in binary bismuth oxides such as

Bi_2O_3 show similar values for Bi atoms.[93−95] The net charges of the stoichiometrically terminated (001)-surface in Figure 6a are already converged to the bulk charges within the outermost layer, indicating equal charge distribution between bulk and surface.

The removal of Cu atoms in the outermost layer increases the net charges of the surrounding Bi and O atoms of at most 0.06 e. The O atoms in the sublayer experience a greater increase in charge transfer of 0.13 e compared to the bulk value. This shows that there is a charge delocalization taking place between the O and Bi atoms in the two outer layers, confirming the states at the Fermi level of the O and Bi atoms in the PDOS in Figure 4. The charge distribution of the other atoms is only weakly disturbed, giving rise to a stable surface composition despite the Cu deficiency. On the contrary, the Bi-deficient surface in Figure 6c shows an increase of the charges for the outermost O atoms by 0.30 e. Additionally, the charges of the outermost Cu atoms and the Bi atoms in the sublayer are slightly higher at 1.10 and 1.73 e, respectively. In the (110) and (100) $Cu/O_{4/4}$-terminated surfaces, the Bader net charges of the O and Cu atoms differ even greater from the bulk values, as shown in the Supporting Information (Figures S10 and S11). The outermost O atoms are undercoordinated, receiving therefore less charge. Thus, the p orbitals of the outermost O atoms are partially unoccupied, generating states above the Fermi level, as shown in the PDOS in Figure 4.
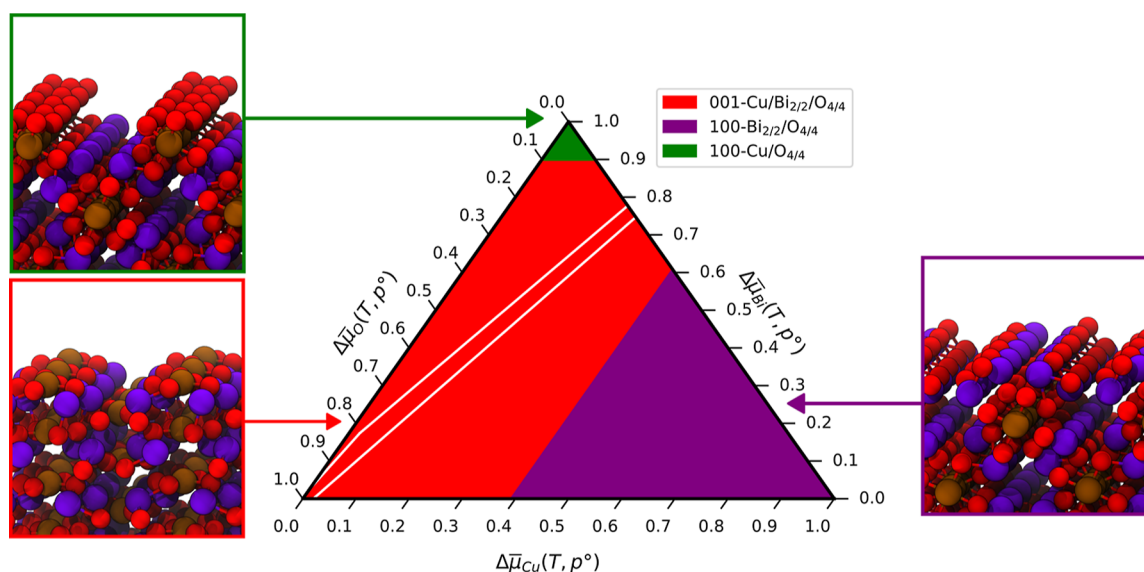
Figure 8. Ternary surface phase diagram for CBO with the stability region and the optimized geometries of the most stable surface terminations.

Besides, Cu terminations indicate a reduction of the outermost Cu atoms as the Bader net charge decreases to 0.49 e. The Bi-terminated surface shows a significant decrease of the Bi atoms's charge transfer by almost 0.80 e, giving rise to a reduction of Bi^{3+} to Bi^{2+} or Bi^{+}. The decrease in the Bader net charge of the Bi atoms in the outermost layer is a consequence of the removed O atoms in this layer. Hence, the Bi atoms have fewer O atoms to distribute their charge, leading to unsaturated coordination and thus partially occupied 6p states, which can be seen in the PDOS in Figure 4d. The Bader net charges for the (110) and (100) surfaces with their terminations are reported in the Supporting Information. The charge distribution of the stoichiometric terminations tends to be almost converged in the outermost layer as well.

Surface Stabilities of CBO and CFO. Figure 7 shows the most stable surface terminations of CFO, comparing the (001), (100), (110), (111), and (012) surfaces, as a function of $\Delta\mu_i = \mu_i - E_i^{GGA+U}$, as defined in eq 4, in a ternary surface phase diagram. The chemical potentials are then normalized by the Gibbs free energy of formation $\Delta\mu_{CFO}^{bulk}$ in eq 8. This leads to

$$0 \leq \Delta\overline{\mu}_i = \frac{n_i \Delta\mu_i}{\Delta\mu_{CFO}^{bulk}} \leq 1 \tag{10}$$

where the stoichiometric coefficient n_i equals 1 for Cu and Fe and 2 for O. The ternary surface phase diagrams of each surface are shown in Figures S12−S19. Additionally, the surface energy values for all investigated surface terminations are reported in Tables S5 and S6. The small region within the white borders is the stability region of the bulk CFO, as presented in Figure 3.

Only the (001)-Fe/O$_{2/2}$, (100)-Cu/O$_{2/2}$, and the (012)-Cu/Fe/O$_{2/2}$ terminations are preferred within the ranges of the chemical potentials. The (001)-Fe/O$_{2/2}$-terminated surface covers a large area in the surface phase diagram for $\Delta\overline{\mu}_{Cu} \in [0.3, 1]$. The stoichiometry of the slab (Cu$_{15}$Fe$_{20}$O$_{40}$) is consistent with the Cu-poor conditions. The (100)−Cu/O$_{2/2}$ surface is only stable at low temperatures in the Cu-rich region. During the optimization of the Cu/O$_{2/2}$-terminated surfaces, the outermost O−Cu−O atoms are arranged perpendicular to the surface, forming a 90-degree

angle. Only at the (100)-Cu/O$_{2/2}$-terminated surface do the neighboring O−Cu−O atoms get too close during the optimization, forming a pyramid-like shape on the surface. Despite the surface reconstructions in the Cu/O$_{2/2}$-terminated surfaces, the surface stability has not increased. This is because Cu is undercoordinated, leading to higher surface energy values.[78] Besides that, the instability of Cu-rich surface terminations is supported by the charge fluctuations across multiple layers and the presence of Cu^{2+} ions within the surface, as shown in the Bader charge analysis in Figure 5. In the ternary surface phase diagram of the (001) surface, a Cu-stoichiometric-terminated surface (Cu$_{24}$Fe$_{24}$O$_{48}$) is only thermodynamically stable under Cu-rich conditions ($\Delta\overline{\mu}_{Cu} \leq 0.05$). Hence, a Cu-terminated surface is only thermodynamically stable if the stoichiometry of the slab is conserved. The (001) surface is the only surface with two different surface terminations, the Cu-stoichiometric, and the Fe/O$_{2/2}$-terminated surface, within the stability region. The Fe/O$_{2/2}$-terminated surface dominates the phase diagram for the other conditions.

In the (110) surface, a small region for a Cu/O$_{2/2}$-terminated surface is shown under Cu- and O-rich conditions ($\Delta\overline{\mu}_{Cu} = 0$ and $\Delta\overline{\mu}_{O} = 0$). According to the stability region in Figure 3, the Cu-based binary oxides are thermodynamically more stable for $\Delta\overline{\mu}_{Cu}$ and $\Delta\overline{\mu}_{O}$ close to 0. As soon as the chemical potential of oxygen decreases (higher temperatures), Fe binary oxides become more stable, as indicated in the stability region of the bulk phase. A large area surrounding the stability region belongs to the stoichiometric-terminated surface, indicating that the stoichiometrically terminated surface is the thermodynamically most stable one for the (110) surface. Under Fe-rich conditions, the Fe/O$_{2/2}$- or Fe/O$_{1/2}$-terminated surfaces are favored, which is also in agreement with the phase stability in Figure 3. When the chemical potential of oxygen is increased to O-rich conditions, the Fe/O$_{2/2}$-terminated surface is more stable than the Fe/O$_{1/2}$-terminated surface. This result is consistent with the stoichiometry of the slabs (Cu$_{18}$Fe$_{24}$O$_{48}$ and Cu$_{18}$Fe$_{24}$O$_{42}$).

The (100) surface represents a narrow area for the stoichiometric termination under Cu-rich conditions. A Cu/

$O_{2/2}$-termination is only stable under Cu- and O-rich conditions. The $Fe/O_{2/2}$-termination covers predominantly the ternary surface phase diagram, proving the high stability under different conditions of $Fe/O_{2/2}$-terminated surfaces.

The ternary surface phase diagrams for the (012) and the (111) surfaces have the same partition as the summarized phase diagram in Figure 7 of all surfaces. Therefore, the stoichiometrically terminated surface is thermodynamically stable. The increased stability of the stoichiometrically terminated and Cu-deficient surfaces is in good agreement with the Bader charge analysis because the charge values in the surface are almost equal to the charge values in the bulk. The (012)-terminated surface is also found to be the preferred orientation in experimental studies using X-ray diffraction and scanning electron microscopy.[96,97] Moreover, theoretical studies indicate higher stability for the (012) surface compared to the (110) surface, which is in agreement with the calculated surface energy values in Table S5.[97]

In general, terminations containing less Cu contribute predominantly to the most stable surfaces for all surface facets. This trend can be seen in a previous study as well.[52]

Figure 8 shows CBO's most stable surface terminations of the (001), (110), and (100) surfaces. The white lines present the stability region described in Figure 3. Here, three different terminations are favored: the (100)-$Cu/O_{4/4}$-, the (100)-$Bi_{2/2}/O_{4/4}$-, and the stoichiometrically terminated (001) surface. Similar to CFO, the surface phase diagram indicates that the stoichiometric-terminated (001) surface is the only thermodynamically stable surface for CBO. The (001) surface has been reported in experimental studies as well.[62,98] Like in CFO, the stoichiometry and the converged charge distributions provide higher stability of the surface. The (100)-$Cu/O_{4/4}$-terminated surface maps a small area in the surface phase diagram under Cu- and O-rich conditions ($\Delta\overline{\mu}_{Cu}$, $\Delta\overline{\mu}_{O} \leq 0.1$). This is in good agreement with the bulk phase stability of the copper oxides, as shown in Figure 3. Unlike CFO, Cu- and $Cu/O_{4/4}$-terminated surfaces are more stable in CBO, confirmed by the weaker Bader net charge fluctuations across multiple layers. In the surface phase diagram for the (100) surface, the Cu- and the $Cu/O_{4/4}$-terminated surfaces are stable under Cu-rich conditions. Furthermore, these two terminations are presented predominantly in the stability region of the (100) surface at higher temperatures. The rest of the diagram is covered by the $Bi_{2/2}/O_{2/4}$- and $Bi_{2/2}/O_{4/4}$-terminated surfaces, as shown in the Supporting Information (S13 and S14).

When $\Delta\overline{\mu}_{Cu}$ is increased to Cu-poor conditions, the $Bi_{2/2}/O_{4/4}$-terminated surface has the lowest surface energy. This trend can be seen for all three surfaces. The Bi/O-terminated surfaces with different Bi/O ratios are predominantly present throughout all three surfaces. The high stability of the $Bi_{2/2}/O_{4/4}$-termination reflects the stability of the Bi oxide bulk phases in Figure 3. Beyond that, the Bader net charge analysis supports the improved stability of Cu-deficient surface terminations by the relatively stable charge values across multiple layers.

CONCLUSIONS

We have investigated the electronic and structural properties of CFO and CBO, using DFT on the PBE + U level. According to the DOS and compared to experiments, the PBE + U is the better approach to describe the semiconducting behavior of

CBO and CFO compared to PBE. Despite the agreement of their electronic properties to experimental studies, the calculated stability region of CFO is larger than that found in experimental studies, indicating the limitations of PBE + U to provide accurate Gibbs free energy of formation values for CFO. The narrow stability region for CBO agrees with the reported experimental results.

The DOS of stoichiometrically-terminated surfaces is similar to the DOS of the corresponding bulk phases. Cation-deficient surface terminations generate midgap states in both materials. The midgap states, formed by atoms in the outermost layer, can be confirmed by the Bader charge analysis. With the help of the Bader charges, we could see fast convergence of charges within the outermost layer of the stable and stoichiometrically terminated surfaces of CFO and CBO. Additionally, charge fluctuations for Fe- or Bi-deficient surface terminations can lead to unstable surfaces. For the (001) surface of CBO, the midgap states are mainly formed by the $[CuO_4]^{6-}$ units in the outer layers. For CFO, the Cu- and Fe-atoms are responsible for the surface states above the Fermi level. Therefore, these sites could be highly reactive in CBO and CFO, respectively.

Furthermore, we have calculated surface energy values for different terminations of the (100), (110), and (001) facets of CBO and (110), (111), (100), (001), and (012) facets of CFO. The surface energy values were compared in ternary surface phase diagrams, including the calculated stability region of the bulk phases of CFO and CBO. The stoichiometrically terminated (001) and (012) surfaces of CBO and CFO, respectively, are the surfaces with the lowest formation energy within the stability region. Cu-deficient surfaces are favored compared to Fe-deficient surfaces in CFO. In CBO, the Cu deficiency is preferred as well.

Combining our results, we propose that the synthesis of these photocathodes has to be considered carefully as cation-deficient surface terminations could limit the PEC performance due to the generated surface states. Moreover, stoichiometry plays a key role in the stability of the photocathode's surface. Our calculations present a solid theoretical analysis of the surface properties of CBO and CFO, providing the theoretical basis for further studies on the catalytic behavior of these interesting materials.

■ ASSOCIATED CONTENT

Data Availability Statement

The data supporting the findings of this study are openly available in Zenodo at 10.5281/zenodo.10679302.

ⓢ Supporting Information

The Supporting Information is available free of charge at https://pubs.acs.org/doi/10.1021/acs.jpcc.4c01330.

> Bulk properties for various values of the U parameter, $\vec{k}$-point grid setting for each surface, surface energy values for all investigated surface terminations, DOS of different surfaces of CBO and CFO, Bader charge analysis of different surfaces of CFO and CBO, ternary surface phase diagrams for each surface of CBO and CFO, and the surface energy values for all analyzed surface terminations of CBO and CFO (PDF)

■ AUTHOR INFORMATION

Corresponding Author

Timo Jacob − *Institute of Electrochemistry, Ulm University, 89081 Ulm, Germany; Helmholtz-Institute Ulm (HIU) for*

Electrochemical Energy Storage, 89081 Ulm, Germany;
Karlsruhe Institute of Technology (KIT), 76021 Karlsruhe,
Germany; orcid.org/0000-0001-7777-2306;
Email: timo.jacob@uni-ulm.de

Authors

Julian Beßner − Institute of Electrochemistry, Ulm University,
89081 Ulm, Germany; orcid.org/0000-0001-9454-3679

Stefanie E. Bogenrieder − Institute of Electrochemistry, Ulm
University, 89081 Ulm, Germany; orcid.org/0009-0006-
9201-4486

Robert Neuhoff − Institute of Electrochemistry, Ulm
University, 89081 Ulm, Germany

Björn Kirchhoff − Institute of Electrochemistry, Ulm
University, 89081 Ulm, Germany; orcid.org/0000-0002-
8600-7806

Complete contact information is available at:
https://pubs.acs.org/10.1021/acs.jpcc.4c01330

Author Contributions

J.B.: conceptualization, investigation, data generation and analysis, visualization, and writing—original draft preparation. S.E.B.: writing—review and editing. R.N.: data generation and analysis. B.K.: supervision and writing—review and editing. T.J.: resources, supervision, and writing—review and editing.

Notes

The authors declare no competing financial interest.

REFERENCES

(1) Lewis, N. S.; Nocera, D. G. Powering the planet: Chemical challenges in solar energy utilization. Proc. Natl. Acad. Sci. U.S.A. 2006, 103, 15729−15735.

(2) Lewis, N. S. Research opportunities to advance solar energy utilization. Science 2016, 351, aad1920.

(3) Tilley, S. D. Recent Advances and Emerging Trends in Photo-Electrochemical Solar Energy Conversion. Adv. Energy Mater. 2019, 9, 1802877.

(4) Gust, D.; Moore, T. A.; Moore, A. L. Solar Fuels via Artificial Photosynthesis. Acc. Chem. Res. 2009, 42, 1890−1898.

(5) Gonzaga, I. L. E.; Mercado, C. C. Copper ternary oxides as photocathodes for solar-driven CO₂ reduction. Rev. Adv. Mater. Sci. 2022, 61, 430−457.

(6) White, J. L.; Baruch, M. F.; Pander, J. E.; Hu, Y.; Fortmeyer, I. C.; Park, J. E.; Zhang, T.; Liao, K.; Gu, J.; Yan, Y.; et al. Light-Driven Heterogeneous Reduction of Carbon Dioxide: Photocatalysts and Photoelectrodes. Chem. Rev. 2015, 115, 12888−12935.

(7) Li, J.; Wu, N. Semiconductor-based photocatalysts and photoelectrochemical cells for solar fuel generation: a review. Catal.: Sci. Technol. 2015, 5, 1360−1384.

(8) Brahms, S.; Nikitine, S.; Dahl, J. P. On the band structure and the absorption spectrum of Cu₂O. Phys. Lett. 1966, 22, 31−33.

(9) Bendavid, L. I.; Carter, E. A. First-Principles Predictions of the Structure, Stability, and Photocatalytic Potential of Cu₂O Surfaces. J. Phys. Chem. B 2013, 117, 15750−15760.

(10) Paracchino, A.; Laporte, V.; Sivula, K.; Grätzel, M.; Thimsen, E. Highly active oxide photocathode for photoelectrochemical water reduction. Nat. Mater. 2011, 10, 456−461.

(11) Hara, M.; Kondo, T.; Komoda, M.; Ikeda, S.; Kondo, J. N.; Domen, K.; Hara, M.; Shinohara, K.; Tanaka, A. Cu₂O as a photocatalyst for overall water splitting under visible light irradiation. Chem. Commun. 1998, No. 3, 357−358.

(12) de Jongh, P. E.; Vanmaekelbergh, D.; Kelly, J. J. Cu₂O: a catalyst for the photochemical decomposition of water? Chem. Commun. 1999, No. 12, 1069−1070.

(13) He, H.; Liao, A.; Guo, W.; Luo, W.; Zhou, Y.; Zou, Z. State-of-the-art progress in the use of ternary metal oxides as photoelectrode materials for water splitting and organic synthesis. Nano Today 2019, 28, 100763.

(14) Rajeshwar, K.; Hossain, M. K.; Macaluso, R. T.; Janáky, C.; Varga, A.; Kulesza, P. J. Review—Copper Oxide-Based Ternary and Quaternary Oxides: Where Solid-State Chemistry Meets Photo-electrochemistry. J. Electrochem. Soc. 2018, 165, H3192−H3206.

(15) Abdi, F. F.; Berglund, S. P. Recent developments in complex metal oxide photoelectrodes. J. Phys. D: Appl. Phys. 2017, 50, 193002.

(16) Liu, X.; Xiao, J.; Ma, S.; Shi, C.; Pan, L.; Zou, J.-J. Review on Bismuth-Based Photocatalyst for CO₂ Conversion. ChemNanoMat 2021, 7, 684−698.

(17) Wu, X.; Toe, C. Y.; Su, C.; Ng, Y. H.; Amal, R.; Scott, J. Preparation of Bi-based photocatalysts in the form of powdered particles and thin films: a review. J. Mater. Chem. A 2020, 8, 15302−15318.

(18) Wang, S.; Wang, L.; Huang, W. Bismuth-based photocatalysts for solar energy conversion. J. Mater. Chem. A 2020, 8, 24307−24352.

(19) Chen, P.; Liu, H.; Cui, W.; Lee, S. C.; Wang, L.; Dong, F. Bi-based photocatalysts for light-driven environmental and energy applications: Structural tuning, reaction mechanisms, and challenges. EcoMat 2020, 2, No. e12047.

(20) He, R.; Xu, D.; Cheng, B.; Yu, J.; Ho, W. Review on nanoscale Bi-based photocatalysts. Nanoscale Horiz. 2018, 3, 464−504.

(21) Fang, W.; Shangguan, W. A review on bismuth-based composite oxides for photocatalytic hydrogen generation. Int. J. Hydrogen Energy 2019, 44, 895−912.

(22) Cooper, J. K.; Zhang, Z.; Roychoudhury, S.; Jiang, C.-M.; Gul, S.; Liu, Y.-S.; Dhall, R.; Ceballos, A.; Yano, J.; Prendergast, D.; et al. CuBi₂O₄: Electronic Structure, Optical Properties, and Photoelectrochemical Performance Limitations of the Photocathode. Chem. Mater. 2021, 33, 934−945.

(23) Sullivan, I.; Zoellner, B.; Maggard, P. A. Copper(I)-Based p-Type Oxides for Photoelectrochemical and Photovoltaic Solar Energy Conversion. Chem. Mater. 2016, 28, 5999−6016.

(24) Oh, Y.; Yang, W.; Kim, J.; Jeong, S.; Moon, J. Enhanced Photocurrent of Transparent CuFeO₂ Photocathodes by Self-Light-Harvesting Architecture. ACS Appl. Mater. Interfaces 2017, 9, 14078−14087.

(25) Read, C. G.; Park, Y.; Choi, K.-S. Electrochemical Synthesis of p-Type CuFeO₂ Electrodes for Use in a Photoelectrochemical Cell. J. Phys. Chem. Lett. 2012, 3, 1872−1876.

(26) Jiang, T.; Zhao, Y.; Liu, M.; Chen, Y.; Xia, Z.; Xue, H. Enhancing the Lifetime of Photoinduced Charge Carriers in CuFeO₂ Nanoplates by Hydrothermal Doping of Mg for Photoelectrochemical Water Reduction. Phys. Status Solidi A 2018, 215, 1800056.

(27) Jin, Y.; Chumanov, G. Solution synthesis of pure 2H CuFeO₂ at low temperatures. RSC Adv. 2016, 6, 26392−26397.

(28) Jiang, C.-M.; Reyes-Lillo, S. E.; Liang, Y.; Liu, Y.-S.; Liu, G.; Toma, F. M.; Prendergast, D.; Sharp, I. D.; Cooper, J. K. Electronic Structure and Performance Bottlenecks of CuFeO₂ Photocathodes. Chem. Mater. 2019, 31, 2524−2534.

(29) Amrute, A. P.; Łodziana, Z.; Mondelli, C.; Krumeich, F.; Pérez-Ramírez, J. Solid-State Chemistry of Cuprous Delafossites: Synthesis and Stability Aspects. Chem. Mater. 2013, 25, 4423−4435.

(30) Fugate, E. A.; Biswas, S.; Clement, M. C.; Kim, M.; Kim, D.; Asthagiri, A.; Baker, L. R. The role of phase impurities and lattice

defects on the electron dynamics and photochemistry of $CuFeO_2$ solar photocathodes. *Nano Res.* **2019**, *12*, 2390−2399.

(31) Baiano, C.; Schiavo, E.; Gerbaldi, C.; Bella, F.; Meligrana, G.; Talarico, G.; Maddalena, P.; Pavone, M.; Muñoz-García, A. B. Role of surface defects in CO_2 adsorption and activation on $CuFeO_2$ delafossite oxide. *Mol. Catal.* **2020**, *496*, 111181.

(32) Hossain, Q. S.; Ahmed, S.; Nishat, S. S.; Hossain, M. Z.; Khan, M. N. I.; Hasan, T.; Bashar, M. S.; Hakim, M.; Syed, I. M.; Hossain, K. S.; et al. An *ab initio* DFT perspective on experimentally synthesized $CuBi_2O_4$. *RSC Adv.* **2023**, *13*, 14291−14305.

(33) Berglund, S. P.; Abdi, F. F.; Bogdanoff, P.; Chemseddine, A.; Friedrich, D.; van de Krol, R. Comprehensive Evaluation of $CuBi_2O_4$ as a Photocathode Material for Photoelectrochemical Water Splitting. *Chem. Mater.* **2016**, *28*, 4231−4242.

(34) Eyert, V.; Frésard, R.; Maignan, A. Long-range magnetic order and spin-lattice coupling in delafossite $CuFeO_2$. *Phys. Rev. B* **2008**, *78*, 052402.

(35) Zheng, H.-S.; Yao, G.-Y.; Zhao, Z.-Y. Microstructure and Electronic Properties of Low-Index Stoichiometric $CuFeO_2$ Surfaces: DFT Calculations. *J. Electron. Mater.* **2022**, *51*, 2316−2336.

(36) Reuter, K.; Scheffler, M. Composition, structure, and stability of $RuO_2(110)$ as a function of oxygen pressure. *Phys. Rev. B* **2001**, *65*, 035406.

(37) Soon, A.; Todorova, M.; Delley, B.; Stampfl, C. Thermodynamic stability and structure of copper oxide surfaces: A first-principles investigation. *Phys. Rev. B* **2007**, *75*, 125420.

(38) Kratzer, P.; Penev, E.; Scheffler, M. Understanding the growth mechanisms of GaAs and InGaAs thin films by employing first-principles calculations. *Appl. Surf. Sci.* **2003**, *216*, 436−446.

(39) Jacob, T. Theoretical investigations on the potential-induced formation of Pt-oxide surfaces. *J. Electroanal. Chem.* **2007**, *607*, 158−166.

(40) Jiang, Y.; Shi, Y.; Xiang, X.; Qi, J.; Han, Y.; Liao, Z.; Lu, T. Thermodynamic Stabilities of Perfect and Vacancy-Defected Li_2TiO_3 (001) Surfaces From First-Principles Analyses. *Phys. Rev. Appl.* **2019**, *11*, 054088.

(41) Allison, T. C. *NIST-JANAF Thermochemical Tables - SRD 13*; National Institute of Standards and Technology, 2013.

(42) Kresse, G.; Joubert, D. From ultrasoft pseudopotentials to the projector augmented-wave method. *Phys. Rev. B* **1999**, *59*, 1758−1775.

(43) Kresse, G.; Furthmüller, J. Efficient iterative schemes for ab initio total-energy calculations using a plane-wave basis set. *Phys. Rev. B* **1996**, *54*, 11169−11186.

(44) Kohn, W.; Sham, L. J. Self-Consistent Equations Including Exchange and Correlation Effects. *Phys. Rev.* **1965**, *140*, A1133−A1138.

(45) Kresse, G.; Furthmüller, J. Efficiency of ab-initio total energy calculations for metals and semiconductors using a plane-wave basis set. *Comput. Mater. Sci.* **1996**, *6*, 15−50.

(46) Kresse, G.; Hafner, J. Ab initio molecular-dynamics simulation of the liquid-metal−amorphous-semiconductor transition in germanium. *Phys. Rev. B* **1994**, *49*, 14251−14269.

(47) Perdew, J. P.; Burke, K.; Ernzerhof, M. Generalized Gradient Approximation Made Simple. *Phys. Rev. Lett.* **1996**, *77*, 3865−3868.

(48) Dudarev, S. L.; Botton, G. A.; Savrasov, S. Y.; Humphreys, C. J.; Sutton, A. P. Electron-energy-loss spectra and the structural stability of nickel oxide: An LSDA + U study. *Phys. Rev. B* **1998**, *57*, 1505−1509.

(49) Fardush Tanha, J.; Farhad, S. F. U.; Honey, U.; Tanvir, N. I.; Hasan, T.; Shahriyar Nishat, S.; Kabir, A.; Ahmed, S.; Hakim, M.; Khan, M. N. I.; et al. A DFT + *U* look into experimentally synthesized monoclinic scheelite $BiVO_4$. *J. Appl. Phys.* **2021**, *130*, 235107.

(50) Matsushima, S.; Yamada, K.; Nakamura, H.; Arai, M.; Kobayashi, K. Electronic structure of Bi_2CuO_4 with antiferromagnetic spin ordering. *J. Ceram. Soc. Jpn.* **2008**, *116*, 589−592.

(51) Oropeza, F. E.; Dzade, N. Y.; Pons-Martí, A.; Yang, Z.; Zhang, K. H. L.; de Leeuw, N. H.; Hensen, E. J. M.; Hofmann, J. P. Electronic

(52) Ferri, M.; Elliott, J. D.; Camellone, M. F.; Fabris, S.; Piccinin, S. $CuFeO_2$-Water Interface under Illumination: Structural, Electronic, and Catalytic Implications for the Hydrogen Evolution Reaction. *ACS Catal.* **2021**, *11*, 1897−1910.

(53) Živković, A.; Roldan, A.; De Leeuw, N. H. Density functional theory study explaining the underperformance of copper oxides as photovoltaic absorbers. *Phys. Rev. B* **2019**, *99*, 035154.

(54) Wang, V.; Xu, N.; Liu, J.-C.; Tang, G.; Geng, W.-T. VASPKIT: A user-friendly interface facilitating high-throughput computing and analysis using VASP code. *Comput. Phys. Commun.* **2021**, *267*, 108033.

(55) Bader, R. F. W. *Atoms in Molecules*; Clarendon Press, 1994; p 438.

(56) Humphrey, W.; Dalke, A.; Schulten, K. VMD − Visual Molecular Dynamics. *J. Mol. Graphics* **1996**, *14*, 33−38.

(57) Schorne-Pinto, J.; Cassayre, L.; Presmanes, L.; Barnabé, A. Insights on the Stability and Cationic Nonstoichiometry of $CuFeO_2$ Delafossite. *Inorg. Chem.* **2019**, *58*, 6431−6444.

(58) Khvan, A. V.; Fabrichnaya, O. B.; Savinykh, G.; Adam, R.; Seifert, H. J. Thermodynamic Assessment of the Cu-Fe-O System. *J. Phase Equilib. Diffus.* **2011**, *32*, 498−511.

(59) Sharma, G.; Zhao, Z.; Sarker, P.; Nail, B. A.; Wang, J.; Huda, M. N.; Osterloh, F. E. Electronic structure, photovoltage, and photo-catalytic hydrogen evolution with p-$CuBi_2O_4$ nanocrystals. *J. Mater. Chem. A* **2016**, *4*, 2936−2942.

(60) Tolba, S. A.; Gameel, K. M.; Ali, B. A.; Almossalami, H. A.; Allam, N. K. The dft+u: Approaches, accuracy, and application. In *Density Functional Calculations*; Yang, G., Ed.; IntechOpen: Rijeka, 2018; Chapter 1.

(61) Cococcioni, M.; de Gironcoli, S. Linear response approach to the calculation of the effective interaction parameters in the LDA + U method. *Phys. Rev. B* **2005**, *71*, 035105.

(62) Jung, H. J.; Lim, Y.; Choi, B.-U.; Bae, H. B.; Jung, W.; Ryu, S.; Oh, J.; Chung, S.-Y. Direct Identification of Antisite Cation Intermixing and Correlation with Electronic Conduction in $CuBi_2O_4$ for Photocathodes. *ACS Appl. Mater. Interfaces* **2020**, *12*, 43720−43727.

(63) Choi, C.; Gu, G. H.; Noh, J.; Park, H. S.; Jung, Y. Understanding potential-dependent competition between electrocatalytic dinitrogen and proton reduction reactions. *Nat. Commun.* **2021**, *12*, 4353.

(64) Troc, R.; Janicki, J.; Filatow, I.; Fischer, P.; Murasik, A. Three-dimensional magnetic properties of Bi_2CuO_4. *J. Phys.: Condens. Matter* **1990**, *2*, 6989−6998.

(65) Galakhov, V. R.; Poteryaev, A. I.; Kurmaev, E. Z.; Anisimov, V. I.; Bartkowski, S.; Neumann, M.; Lu, Z. W.; Klein, B. M.; Zhao, T.-R. Valence-band spectra and electronic structure of $CuFeO_2$. *Phys. Rev. B* **1997**, *56*, 4584−4591.

(66) Mekata, M.; Yaguchi, N.; Takagi, T.; Mitsuda, S.; Yoshizawa, H. Magnetic ordering in delafossite $CuFeO_2$. *J. Magn. Magn. Mater.* **1992**, *104−107*, 823−824.

(67) Janson, O.; Kuzian, R. O.; Drechsler, S.-L.; Rosner, H. Electronic structure and magnetic properties of the spin-1/2 Heisenberg magnet Bi_2CuO_4. *Phys. Rev. B* **2007**, *76*, 115119.

(68) Di Sante, D.; Hausoel, A.; Barone, P.; Tomczak, J. M.; Sangiovanni, G.; Thomale, R. Realizing double Dirac particles in the presence of electronic interactions. *Phys. Rev. B* **2017**, *96*, 121106.

(69) Guo, S.-D. X-ray emission spectra and gaps of $CuFeO_2$ with the modified Becke−Johnson potential. *J. Magn. Magn. Mater.* **2015**, *377*, 226−228.

(70) Husek, J.; Cirri, A.; Biswas, S.; Asthagiri, A.; Baker, L. R. Hole Thermalization Dynamics Facilitate Ultrafast Spatial Charge Separation in $CuFeO_2$ Solar Photocathodes. *J. Phys. Chem. C* **2018**, *122*, 11300−11304.

(71) Hermans, Y.; Klein, A.; Sarker, H. P.; Huda, M. N.; Junge, H.; Toupance, T.; Jaegermann, W. Pinning of the Fermi Level in $CuFeO_2$

by Polaron Formation Limiting the Photovoltage for Photochemical Water Splitting. *Adv. Funct. Mater.* **2020**, *30*, 1910432.

(72) Schiavo, E.; Latouche, C.; Barone, V.; Crescenzi, O.; Muñoz-García, A. B.; Pavone, M. An *ab initio* study of Cu-based delafossites as an alternative to nickel oxide in photocathodes: effects of Mg-doping and surface electronic features. *Phys. Chem. Chem. Phys.* **2018**, *20*, 14082−14089.

(73) Ye, F.; Ren, Y.; Huang, Q.; Fernandez-Baca, J. A.; Dai, P.; Lynn, J. W.; Kimura, T. Spontaneous spin-lattice coupling in the geometrically frustrated triangular lattice antiferromagnet $CuFeO_2$. *Phys. Rev. B* **2006**, *73*, 220404.

(74) Zhao, T.-R.; Hasegawa, M.; Takei, H. Crystal growth and characterization of cuprous ferrite ($CuFeO_2$). *J. Cryst. Growth* **1996**, *166*, 408−413.

(75) Piccinin, S.; Stampfl, C.; Scheffler, M. First-principles investigation of Ag-Cu alloy surfaces in an oxidizing environment. *Phys. Rev. B* **2008**, *77*, 075426.

(76) Lany, S. Semiconductor thermochemistry in density functional calculations. *Phys. Rev. B* **2008**, *78*, 245207.

(77) Patton, D. C.; Porezag, D. V.; Pederson, M. R. Simplified generalized-gradient approximation and anharmonicity: Benchmark calculations on molecules. *Phys. Rev. B* **1997**, *55*, 7454−7459.

(78) Wang, L.; Zhou, F.; Meng, Y. S.; Ceder, G. First-principles study of surface properties of $LiFePO_4$: Surface energy, structure, Wulff shape, and surface redox potential. *Phys. Rev. B* **2007**, *76*, 165435.

(79) Ferri, M.; Elliott, J.; Farnesi Camellone, M.; Fabris, S.; Piccinin, S. Thermodynamic Stability and Native Point Defects of $CuFeO_2$ Photocathodes in Dry and Electrochemical Environments. *J. Phys. Chem. C* **2019**, *123*, 29589−29598.

(80) Carvalho, M.-L.; Styve, V. J.; Meen, J. K.; Elthon, D. Phase equilibria of the bismuth oxide−calcium oxide−copper oxide system at 1 atm of pure oxygen. *Phys. C* **2000**, *336*, 1−9.

(81) Strejc, A.; Sedmidubský, D.; Růžička, K.; Leitner, J. Thermochemical properties of Bi_2CuO_4. *Thermochim. Acta* **2003**, *402*, 69−74.

(82) Tsang, C.-F.; Meen, J. K.; Elthon, D. Phase Equilibria of the Bismuth Oxide-Copper Oxide System in Oxygen at 1 atm. *J. Am. Ceram. Soc.* **1994**, *77*, 3119−3124.

(83) Wolff, N.; Klimm, D.; Habicht, K.; Fritsch, K. Crystal growth and thermodynamic investigation of $Bi_2M^{2+}O_4$ (M = Pd, Cu). *CrystEngComm* **2021**, *23*, 3230−3238.

(84) Hallstedt, B.; Risold, D.; Gauckler, L. J. Thermodynamic Evaluation of the Bi-Cu-O System. *J. Am. Ceram. Soc.* **1996**, *79*, 353−358.

(85) Paudel, T. R.; Jaswal, S. S.; Tsymbal, E. Y. Intrinsic defects in multiferroic $BiFeO_3$ and their effect on magnetism. *Phys. Rev. B* **2012**, *85*, 104409.

(86) Henmi, C. Kusachiite, $CuBi_2O_4$, a new mineral from Fuka, Okayama Prefecture, Japan. *Mineral. Mag.* **1995**, *59*, 545−548.

(87) Farhad, S. F. U.; Naher, M. I.; Tanvir, N. I.; Quddus, M. S.; Jahan, S. A.; Islam, S.; Shaikh, M. A. A. A facile top-down synthesis of phase pure $CuBi_2O_4$ photocathode materials by low-energy sequential ball milling. 2023, ArXiv (Cornell University) https://doi.org/10.48550/arXiv.2209.08530 (accessed May 09, 2024).

(88) Hossain, M. K.; Samu, G. F.; Gandha, K.; Santhanagopalan, S.; Liu, J. P.; Janáky, C.; Rajeshwar, K. Solution Combustion Synthesis, Characterization, and Photocatalytic Activity of $CuBi_2O_4$ and Its Nanocomposites with CuO and α-Bi_2O_3. *J. Phys. Chem. C* **2017**, *121*, 8252−8261.

(89) Noguera, C. Polar oxide surfaces. *J. Phys.: Condens. Matter* **2000**, *12*, R367−R410.

(90) Kramer, D.; Ceder, G. Tailoring the Morphology of $LiCoO_2$: A First Principles Study. *Chem. Mater.* **2009**, *21*, 3799−3809.

(91) Maimaiti, Y.; Nolan, M.; Elliott, S. D. Reduction mechanisms of the CuO(111) surface through surface oxygen vacancy formation and hydrogen adsorption. *Phys. Chem. Chem. Phys.* **2014**, *16*, 3036.

(92) Yang, X.; Fugate, E. A.; Mueanngern, Y.; Baker, L. R. Photoelectrochemical CO_2 Reduction to Acetate on Iron−Copper Oxide Catalysts. *ACS Catal.* **2017**, *7*, 177−180.

(93) Lei, Y.-H.; Chen, Z.-X. Density functional study of the stability of various α-Bi_2O_3 surfaces. *J. Chem. Phys.* **2013**, *138*, 054703.

(94) Lucid, A.; Iwaszuk, A.; Nolan, M. A first principles investigation of Bi_2O_3-modified TiO_2 for visible light Activated photocatalysis: The role of TiO_2 crystal form and the Bi^{3+} stereochemical lone pair. *Mater. Sci. Semicond. Process.* **2014**, *25*, 59−67.

(95) Xie, L.; Li, L.; Heikes, C. A.; Zhang, Y.; Hong, Z.; Gao, P.; Nelson, C. T.; Xue, F.; Kioupakis, E.; Chen, L.; et al. Giant Ferroelectric Polarization in Ultrathin Ferroelectrics via Boundary-Condition Engineering. *Adv. Mater.* **2017**, *29*, 1701475.

(96) Omran Alkhayatt, A. H.; Thahab, S. M.; Zgair, I. A. Structure, surface morphology and optical properties of post-annealed delafossite $CuFeO_2$ thin films. *Optik* **2016**, *127*, 3745−3749.

(97) Dai, C.; Tian, X.; Nie, Y.; Lin, H.-M.; Yang, C.; Han, B.; Wang, Y. Surface Facet of $CuFeO_2$ Nanocatalyst: A Key Parameter for H_2O_2 Activation in Fenton-Like Reaction and Organic Pollutant Degradation. *Environ. Sci. Technol.* **2018**, *52*, 6518−6525.

(98) Yamada, K.; Takada, K.-i.; Hosoya, S.; Watanabe, Y.; Endoh, Y.; Tomonaga, N.; Suzuki, T.; Ishigaki, T.; Kamiyama, T.; Asano, H.; Izumi, F. Three-Dimensional Antiferromagnetic Order and Aniso-tropic Magnetic Properties in Bi_2CuO_4. *J. Phys. Soc. Jpn.* **1991**, *60*, 2406−2414.